Optical Materials 133 (2022) 112967

Contents lists available at ScienceDirect

Optical Materials

journal homepage: www.elsevier.com/locate/optmat

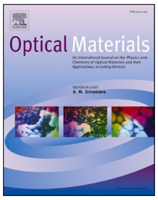

Research Article

Thickness-dependent magnetooptical properties of ion beam sputtered polycrystalline $Ce_1Y_2Fe_5O_{12}$ films

Yuki Yoshihara [a,b,c], Tomoya Sugita [d], Pang Boey Lim [c], Yasuyuki Tamba [d], Hiroaki Inoue [d], Kazushi Ishiyama [a], Mitsuteru Inoue [a], Caroline A. Ross [e], Taichi Goto [a,*]

[a] *Research Institute of Electrical Communication, Tohoku University, 2-1-1 Katahira, Aoba, Sendai, Miyagi, 980-8577, Japan*
[b] *Graduate School of Engineering, Tohoku University, 6-6 Aramaki, Aoba, Sendai, Miyagi, 980-8579, Japan*
[c] *Toyohashi University of Technology, 1-1 Hibarigaoka, Tempaku, Aichi, 441-8580, Japan*
[d] *Kyocera Corporation, 3-7-1 Minatomirai, Nishi, Yokohama, Kanagawa, 220-0012, Japan*
[e] *Department of Materials Science and Engineering, Massachusetts Institute of Technology, 77 Massachusetts Avenue, Cambridge, MA, 02139, United States*

ARTICLE INFO

Keywords:
Ce
YIG
Magnetooptical properties
Magnetic properties
Crack
XRD
XPS
TEM
Thickness dependence
Ceria

ABSTRACT

Polycrystalline cerium-substituted yttrium iron garnet (Ce:YIG, $Ce_1Y_2Fe_5O_{12}$) films were deposited on synthetic fused silica substrates with various thicknesses using ion beam sputtering, and their roughness, transmissivity, optical constants, microstructure, and their magnetic and magnetooptical properties were measured. Thicker films exhibit cracking due to thermal mismatch stress. A ~5 nm thick amorphous layer was observed at the interface between Ce:YIG and the substrates, resulting in a non-monotonic thickness dependence of the measured properties. A 338 nm thick Ce:YIG film showed the largest magnetooptical figure of merit defined as the ratio of Faraday rotation angle to absorption coefficient, 127°/dB at a wavelength of 1550 nm, more than three times larger than prior work.

1. Introduction

Magnetooptical garnet films have been used in many applications including optical sensors, switches, displays and isolators [1–9]. Applications, such as magnetooptical hologram media [4], visualizers for electromagnetic signals [3,6], small-pixel spatial light modulators [7], and on-chip optical isolators [5,10–15], take advantage of the isotropic behavior of polycrystalline magnetooptical garnets which are fabricated on non-garnet substrates including glass, silicon, and silicon on insulator. Several optical isolators have been demonstrated using cerium substituted yttrium iron garnet (Ce:YIG) as a magnetooptical material [16–20] because of its large Faraday rotation (FR) and low absorption at near-infrared (NIR) wavelengths. In earlier publications [12,13,17], film thicknesses of Ce:YIG were targeted at ~200 nm which is suitable for the magnetooptical cladding of waveguides in a NIR on-chip optical isolator. However, other magnetooptical devices require thicker films, such as spatial light modulators [21–23] operating at NIR wavelengths [24], and magnetooptical Q-switches [2,25,26] for compact high-power lasers [27,28] in which the light propagates perpendicular to the magnetooptical film. Recent studies [13,14,20] have improved the quality of polycrystalline Ce:YIG, but enhancing FR for next generation applications is challenging, and the dependence of the magnetooptical properties of Ce:YIG over a wide range of film thickness has not been reported.

In this study, we prepared ten Ce:YIG films with various thicknesses using radio-frequency (RF) ion beam sputtering (IBS) and vacuum annealing [12,17], and we characterized the thickness dependence of the structure and the magnetooptical and magnetic properties using stylus profilometry, x-ray diffraction (XRD), photospectrometry, magnetooptical measurements, vibrating sample magnetometry (VSM), x-ray photoelectron spectroscopy (XPS), and transmission electron microscopy (TEM). The magnetooptical figure of merit (FOM) was calculated and compared with other works. The effects of an interfacial layer between the film and the substrate were investigated to clarify the thickness dependence of the properties.

---

* Corresponding author.
E-mail address: taichi.goto.a6@tohoku.ac.jp (T. Goto).

https://doi.org/10.1016/j.optmat.2022.112967
Received 4 August 2022; Received in revised form 1 September 2022; Accepted 2 September 2022

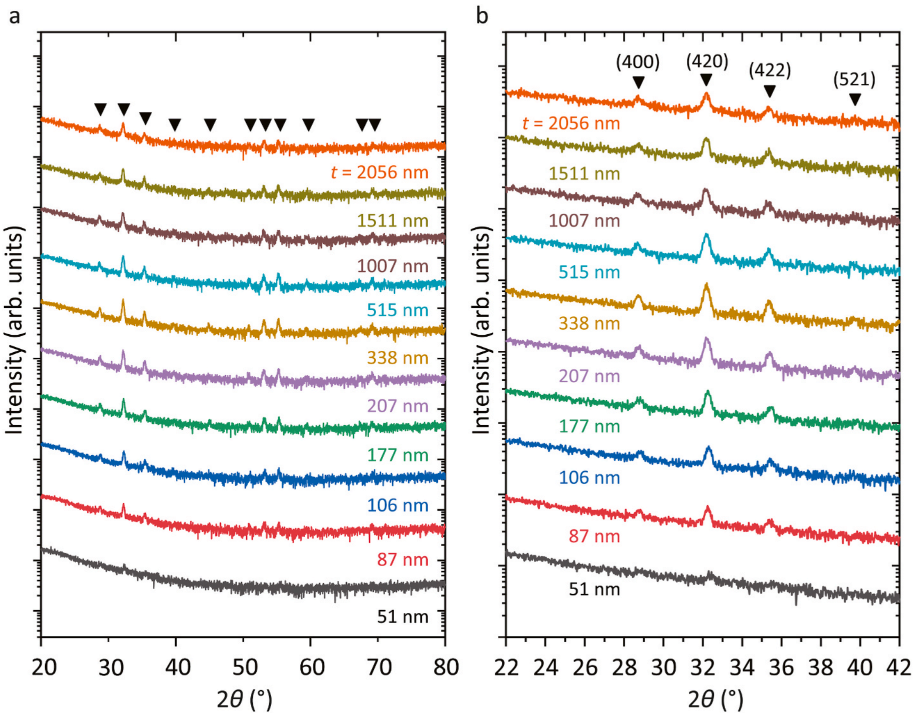

Fig. 1. (a) Grazing incidence XRD $\omega-2\theta$ scan of the prepared samples with various thicknesses t. The incident angle was fixed at $\omega = 0.7°$. The black triangles indicate the peak positions of YIG. (b) Enlarged figure of (a) in the vicinity of the strong peaks.

2. Experimental methods

The substrates consisted of double-side polished 1-inch diameter 0.7 mm thick synthetic-fused-silica substrates (with no anti-reflection coating) and 1-inch diameter 0.725 mm thick Si (100)-oriented substrates with native oxide, and cleaned by sonication using acetone, isopropanol, and deionized water. The samples deposited on the Si substrates were used as references and for characterization of charging effects. Samples were cut into 5 mm × 5 mm using a dicing saw (Disco, DAD321). Films were deposited using an RF IBS deposition system (RMTec, RM17-0010). The base pressure before the deposition was 3.0 $\times$ 10^{-4} Pa and the working pressure was 9.0 $\times$ 10^{-2} Pa. Substrate temperature was held at 200 °C with a heater, and 8-sccm O_2 gas was blown onto the samples, which were rotated during deposition. A 4-inch diameter sintered target with a Cu backing plate and water cooling was used. The composition of the target was nominally $Ce_{1.0}Y_{2.5}Fe_{5.0}O_{12}$ (Kojundo Chemical) which yields a stoichiometric garnet film as described below. The ion gun beam voltage was 800 V, and the beam current was 36 mA. 10 sccm Ar flowed to both the ion gun and low-frequency neutralizer (LFN). The ion beam accelerator voltage was 160 V, and RF power was 75 W. The deposition rate was 1.45 nm/min. The as-deposited film was amorphous, and then the sample was annealed in a rapid thermal annealing system (Ulvac, SSA-P610CP) with a glass chamber as described previously [17]. The working pressure during annealing was 2 Pa, and no gases were introduced into the chamber. The heating speed was 1292 °C/min (i.e., it took 0.6 min to heat from 25 to 800 °C). The sample temperature was held at 800 °C for 20 min and cooled at −214 °C/min from 800 to 550 °C and −21 °C/min from 550 to 100 °C. The temperature change during cooling is shown in Fig. S1 in the Supporting Information.

Sample thickness t was measured using a diamond stylus profilometer (Kosaka Laboratory, ET4000 M). The stylus tip radius and taper angles were 2 μm and 60°. The surface roughness was measured using the same stylus profilometer, and the surface was imaged by optical microscopy. The stylus force of the profilometer was 5 μN, and the scan speed was 0.1 mm/s. The root-mean-square roughness R_q was obtained from scans with the cutoff values and evaluation lengths shown in Table S1.

Composition was measured using energy-dispersive x-ray spectroscopy (EDS, Ametek EDAX Genesis APEX2 Octane) mounted to a low vacuum scanning electron microscope (SEM, Hitachi High Technologies SU 3500). The acceleration voltage was 20 kV, and emission current was 93 μA. The working distance was 10 mm. The ZAF method was used for quantitative correction, which eliminated the influence of the atomic number effect, the absorption effect, and the fluorescence excitation effect on the characteristic x-ray peak intensities. The Ce:YIG films on silicon substrates were fixed by silver paste and carbon tape to eliminate charging. XPS (Ulvac-Phi, Quantera AXM-CI) was used to obtain composition along the thickness direction. The x-ray output current was 100 μA, the voltage was 15 kV, and the power was 25W. The sample was etched using Ar with the acceleration voltage of 1 kV. The obtained data was analyzed using CasaXPS [29] version 2.3. The background effect was eliminated using the Shirley method.

Crystal structure was characterized by XRD using a Rigaku Smartlab in grazing incidence geometry. The x-ray source was a 2 kW Cu Kα1 radiation source with a wavelength of 0.15418 nm. A one-dimensional x-ray detector (D/teX, Ultra 250) was used. The incident angle of the x-ray ω was set to 0.7°, and the parallel soller slit collimator (PSC) angle was 5.0°. The incident slit (IS) width and length were 1.0 mm and 10.0 mm, respectively. The first receiving slit (RS1) and second receiving slit (RS2) widths were 20 mm, and the parallel soller slit analyzer (PSA) angle was 0.5°. The detector scan speed was 4.0°/min without an attenuator, and the data recording angle resolution was 0.02° in continuous scan mode. Lattice parameters were determined using the Rigaku PDXL2 analysis software.

Optical transmissivity was measured with a spectrophotometer (Shimadzu, UV-3150). The optical source is a double-monochromated randomly polarized lamp, with a spot diameter at the sample surface of 2.2 mm. The light was incident perpendicular to the sample. A slow scan speed and 8 nm wavelength resolution were used.

FR and Faraday ellipticity (FE) spectra were measured using a magnetooptical measurement system (JASCO, J-1700FK). The rotating

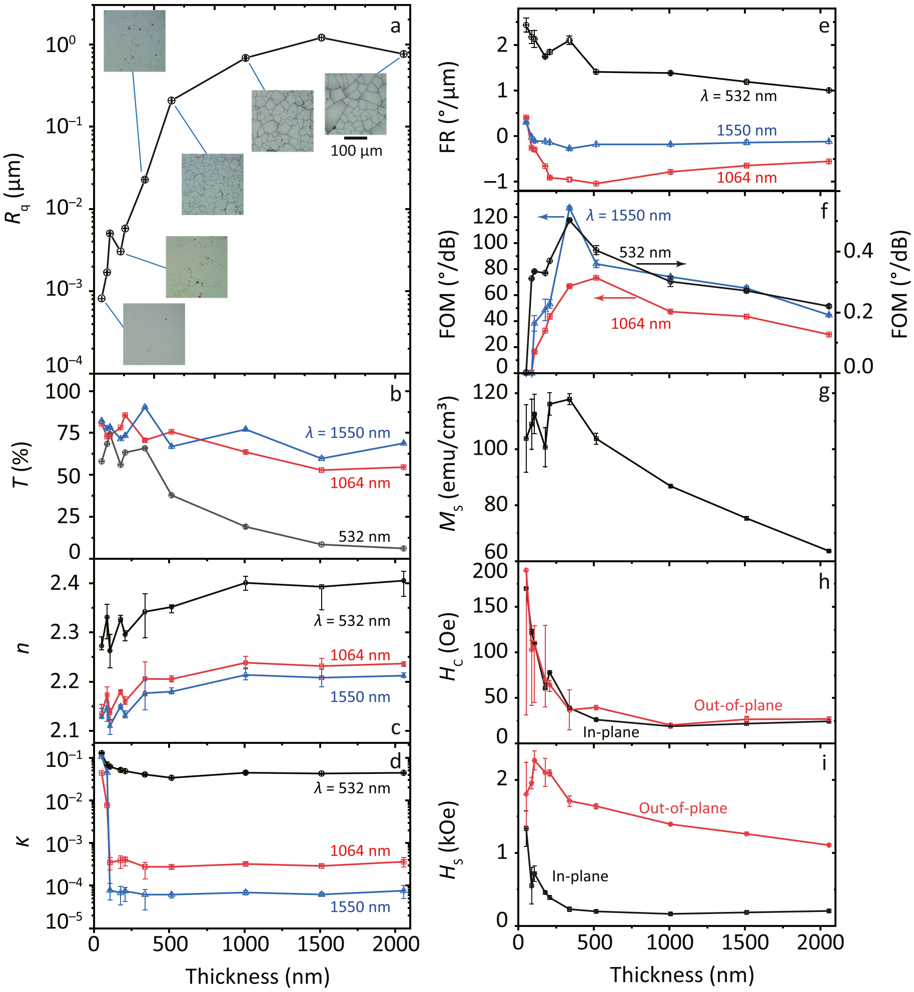

Fig. 2. Thickness dependence of (a) the roughness R_q of the films, (b) transmissivity T of the film/substrates, (c) the refractive index n of the films, (d) the extinction coefficient κ of the films, (e) Faraday rotation (FR) of the film/substrates, (f) figure of merit (FOM) of the films. That of (g) the saturation magnetization M_s, (h) the coercivity H_c, and (i) the saturation magnetic field H_s of the films. (a) Inset images show optical micrographs of the samples.

polarizer and polarization modulation methods were combined for these measurements. The sample temperature was held at 40 ± 0.5 °C using a Peltier temperature controller because of the strong temperature dependence of Ce:YIG magnetization. Photomultiplier and InGaAs-based optical detectors were used for visible and NIR wavelengths, respectively. The resolution of FR and FE were <0.01° and <0.1°, respectively. The spot size of the light at the sample surface was 1 mm × 5 mm and a magnetic field of ±0.5 T was applied.

Magnetic hysteresis loops were measured using a VSM (Tamakawa TM-VSM261483). TEM (JEOL JEM-ARM200F) cross-sectional images were obtained for films grown on a Si substrate to avoid charging.

3. Results and discussion

The thicknesses t of the ten samples were 51 ± 1.1, 87 ± 2.8, 106 ± 4.7, 177 ± 1.4, 207 ± 2.5, 338 ± 7.9, 515 ± 1.9, 1007 ± 5.5, 1511 ± 12.5, and 2056 ± 4.3 nm, with the error representing the standard deviation of ten repeated measurements. Films grown on silicon substrates had almost the same thicknesses as those on fused silica. The composition of the films can be written (normalized to Fe = 5.0) as $Ce_{1\pm0.02}Y_{2\pm0.02}Fe_5O_{12-\delta}$, where δ represents oxygen deficiency (not measured), and the error is the standard deviation of ten EDS measurements at different positions.

From the XRD scans, Fig. 1a and b, most of the samples showed an untextured polycrystalline garnet structure [30] without secondary phases, though the peaks of the 51 nm thick sample were weak and only some of them could be resolved. The lattice constant of the polycrystalline Ce:YIG was 1.243 ± 0.001 nm, 0.012 nm larger than that of YIG because of the larger ionic radius of Ce^{3+} (0.112 nm) compared with Y^{3+} (0.104 nm).

The measured roughness R_q is shown in Fig. 2a with optical microscopy images as insets. R_q increased with thickness and saturated in the range of $t > 1$ μm. This corresponds to the onset of cracking seen in the optical micrographs at $t > 515$ nm. These cracks, with spacing ~10–100 μm, are caused by the large difference in thermal expansion between the film and substrate [12]. The thermal expansion coefficients of garnet (YIG) [31] is 2.5 × 10^{-5} K^{-1} between 23 and 280 °C and 1.0 × 10^{-5} K^{-1} between 280 and 1125 °C, and that of synthetic fused silica [32] is 6 × 10^{-7} K^{-1}. The Ce:YIG is therefore in a state of in-plane tension after cooling which leads to cracks in thicker films. Parts of the film then delaminate leading to the high roughness values.

Transmissivity for the film/substrates with various film thicknesses was measured (Fig. S2a), and Fig. 2b shows the transmissivity versus thickness at three different wavelengths λ. The transmissivity generally decreases with increasing thickness. The deviation of the transmissivity was caused by the phase interference generated at the surface of the film and the interface between the film and substrate. The optical constants comprising the refractive index n and extinction coefficient κ of samples and substrates were obtained using the fringes of the transmission spectra, Fig. 3a and b (also separately plotted in Fig. S2) using fitting and

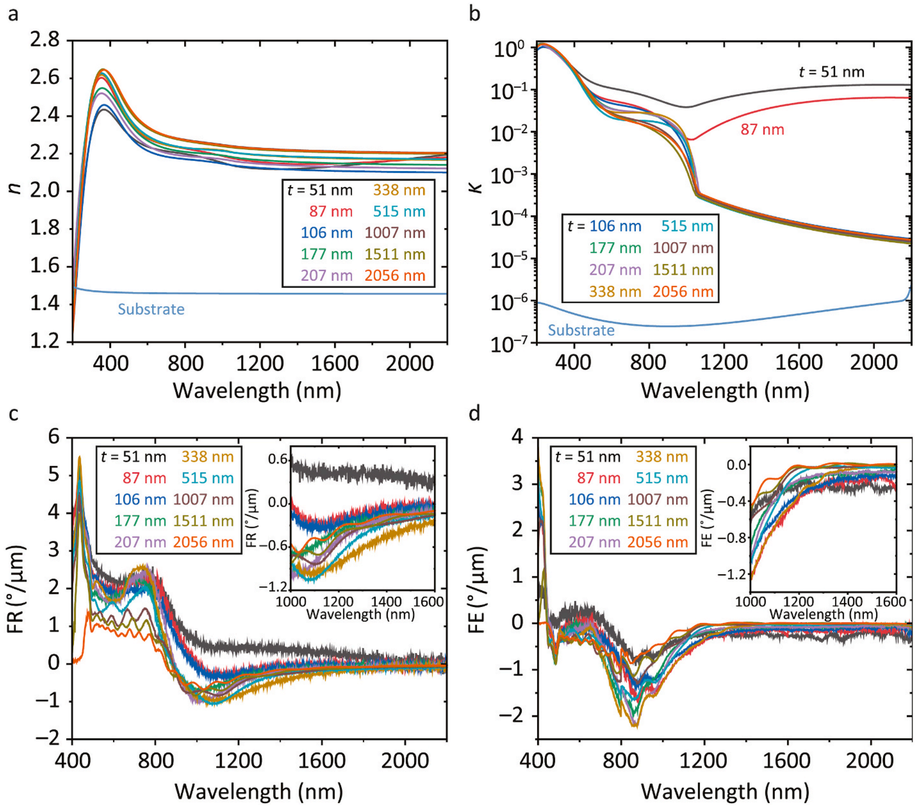

Fig. 3. (a) The refractive index *n* and (b) the extinction coefficient *κ* of the films. (c) Faraday rotation (FR), and (d) Faraday ellipticity (FE) angle spectra of the film/substrates with various sample thicknesses *t*. The individual data are shown separately in Figs. S2 and S4.

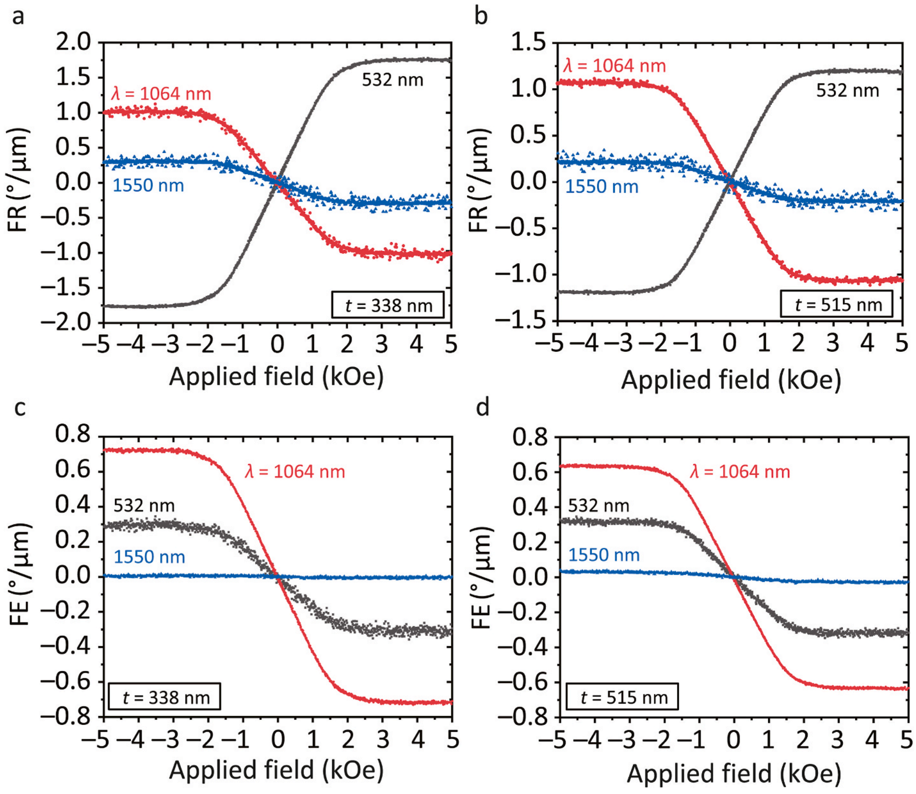

Fig. 4. (a)(b) Faraday rotation (FR) loops of 338 and 515 nm thick samples including substrates at the wavelengths of $\lambda = 532$, 1064, and 1550 nm. (c)(d) Faraday ellipticity (FE) loops of the same samples including substrates.

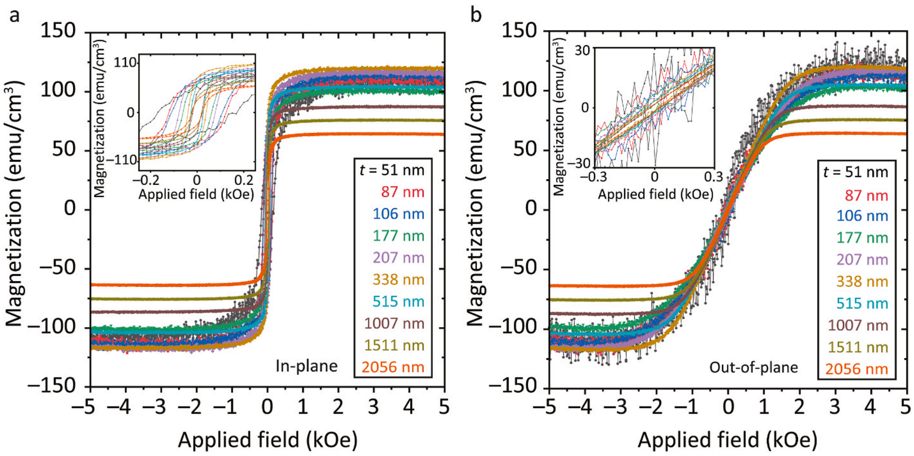

Fig. 5. (a) In-plane and (b) out-of-plane magnetic hysteresis loops of the films with various thicknesses. Insets show the plots near zero field. The paramagnetic components due to the substrates or sample holder were subtracted from the raw data.

simulation software (W. Theiss Hard- and Software, SCOUT version 3.04) [17] based on the Fresnel equation. Previous studies have used this method, showing good agreement between calculation and experiments [20,33]. The fitting model for the thin samples $t \leq 338$ nm was a film/substrate, but the model for the thick samples $t \geq 515$ nm included an additional layer above the film representing the surface roughness, i.e. the model structure consisted of rough layer/film/substrate. The spectra of n and κ, and the thickness of the rough layer determined by the simulation are shown in Fig. S3 and Table S2. Fig. 2c and d summarize the thickness dependence of n and κ at three wavelengths. The value of n slightly increased with t, but the value of κ was independent of thickness except for a dramatic increase for the thinnest film with $t \leq 87$ nm. This is interpreted as indicating an additional layer at the interface between the garnet film and the silica substrate, which will be discussed later. Since κ did not decrease at $t \geq 515$ nm, the reduction of transmissivity for thicker films was attributed to film cracking. Absorption coefficient α, given by α (dB/cm) = 10 × log10[exp(4πκ × 0.01/λ)] at $\lambda = 1550$ nm was 2.17×10^{-3} dB/μm for $t = 338$ and 515 nm, comparable to the previously reported value 4.8×10^{-3} dB/μm [17].

Fig. 3c and d (also separately plotted in Fig. S4) show the FR and FE spectra, where the sign of the direction of FR or FE was positive when a clockwise direction of rotation angle is obtained looking towards the light source from the detector [34]. The observed fringes were caused by film interference. The rotation angle increased as the thickness increased (Fig. 2e), but rotation angle normalized to thickness was not constant because of the film cracking and delamination at $t \geq 515$ nm. Hysteresis loops of FR and FE were also measured at wavelengths of $\lambda = 532$, 1064, and 1550 nm (Fig. 4). The largest FR was obtained with 515 nm thick Ce:YIG, 1.19°/μm, −1.07°/μm, and −0.21°/μm at $\lambda = 532$, 1064, and 1550 nm, respectively. These values were comparable with previously reported values of polycrystalline Ce:YIG without YIG seed layer, −0.13°/μm [5] and –0.27°/μm [17] at $\lambda = 1550$ nm. However, the measured value was smaller than that of bulk single crystalline Ce:YIG, −0.38°/μm [35] and polycrystalline Ce:YIG prepared by two-step-deposition, −0.36°/μm [13] at $\lambda = 1550$ nm. As shown in Fig. 4d, the FEs of the 515 nm thick Ce:YIG at $\lambda = 532$, 1064, and 1550 nm were 0.32, 0.64, and 0.03°/μm, respectively, compared to the previously reported values: 0.27 [16] and 0.06°/μm [36] at $\lambda = 1550$ nm.

The magnetooptical FOM, defined as the FR (°/μm) divided by absorption (dB/μm), was used to evaluate the thickness dependent

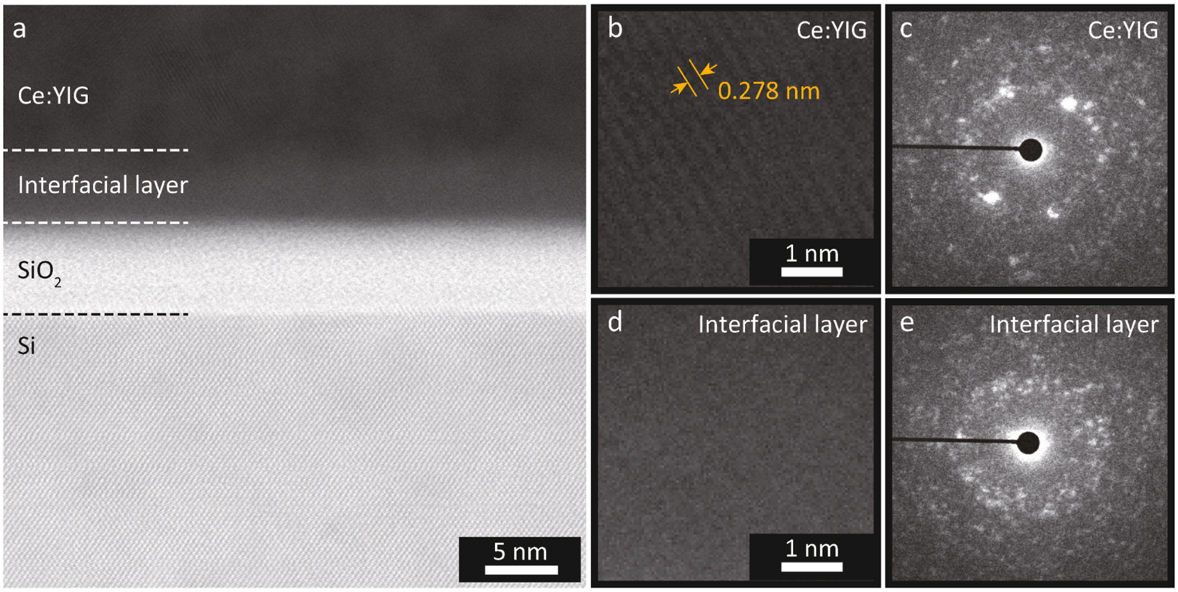

Fig. 6. (a) Cross-sectional TEM image of 515 nm thick sample. (b) A high-resolution image and (c) the electron beam diffraction pattern of the Ce:YIG layer. (d)(e) High resolution image and diffraction pattern from the interfacial layer.

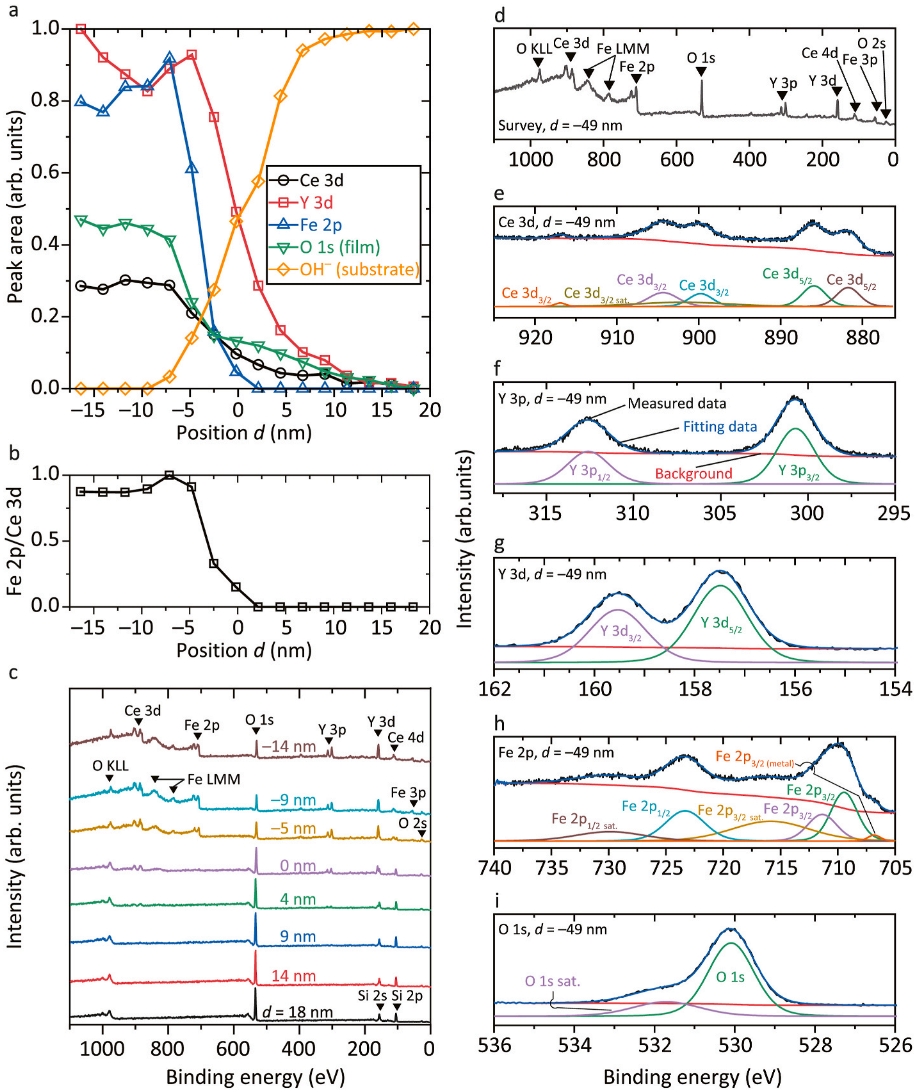

Fig. 7. (a) Element profile along the thickness direction *d*, measured by XPS. (b) The depth dependence of the ratio Fe 2p/Ce 3d. (c) The XPS at various depths. (*d*–i) XPS profile measured at the etched top surface of the sample for (d) survey scan, (e) Ce 3d, (f) Y 3p, (g) Y 3d, (h) Fe 2p, and (i) O 1s.

performance of Ce:YIG. The FOM is highest for $t = 300$–500 nm (Fig. 2f), decreasing at low thickness due to the high absorption, and at the high thicknesses due to cracking-induced loss in FR. The 515 nm thick Ce:YIG showed the largest FOM of 73°/dB at $\lambda = 1064$ nm. The 338 nm thick film showed a FOM of 127°/dB at $\lambda = 1550$ nm, compared to the value of 340°/dB for a single crystalline Ce:YIG [35,37] and values for polycrystalline Ce:YIG films, 20°/dB [38], 37°/dB [13], and 38°/dB [37]. These values might be improved further by increasing the oxygen flow during deposition, as Du et al. demonstrated [14].

Fig. 5a and b (also separately plotted in Fig. S5) show the in-plane and out-of-plane magnetization loops, and Fig. 2g, h, and 2i show the thickness dependences of the saturation magnetization M_s, the coercivity H_c, and the saturation magnetic field H_s, respectively. The H_s was defined as the magnetic field at which the magnetization reached 90% of M_s. The largest value of $M_s = 118$ emu cm^{-3} was obtained at $t = 338$ nm, close to other reported values [17,37,39] of 120 emu cm^{-3}. However, M_s decreases below this value for $t > 500$ nm, which is attributed to cracking and subsequent delamination of parts of the films. Taking $M_s = 118$ emu cm^{-3} and $H_s = 1.7$ kOe from the out-of-plane (hard axis) loop at $t = 338$ nm, an estimate of total anisotropy $K_{\text{total}} = H_s M_s/2 = 1.0 \times 10^5$ erg cm^{-3} (10 kJ m^{-3}) of which 8.7 kJ m^{-3} originates from shape anisotropy [40] and the remainder is assumed to be magnetoelastic anisotropy.

For the thinnest films the M_s decreased, consistent with the presence of an interfacial layer with lower magnetization. The M_s of the as-deposited (amorphous) 51 nm thick film was 26 ± 13 emu cm^{-3} (Fig. S6) compared to $M_s = 104 \pm 4$ emu cm^{-3} for the annealed film. Assuming that the annealed film includes an amorphous layer with magnetization of 26 emu cm^{-3}, we estimate its thickness as ~7.8 nm. This value could range between 4.9 nm and 11.6 nm due to the uncertainty in the values of M_s used in the calculation.

XPS and TEM were used to identify and characterize the interfacial layer. TEM images of the sample with $t = 515$ nm on Si are shown in Fig. 6a. The high-resolution TEM image showed a stack consisting of Ce:YIG/interfacial layer/SiO$_2$/Si substrate. The Ce:YIG layer had crystalline grains; the one shown in Fig. 6b has a lattice spacing of ~0.278 ± 0.007 nm, close to the (420) interplanar spacing of 0.277 nm of YIG [30]. In addition, the electron beam diffraction pattern (Fig. 6c) obtained in the Ce:YIG area showed diffraction spots. The thickness of the interfacial layer was 5.3 ± 0.7 nm, and did not show lattice contrast (Fig. 6d); its electron beam diffraction pattern (Fig. 6e) did not show diffraction spots. Hence, the interfacial layer was amorphous.

Fig. 7a shows the XPS semiquantitative analysis depth profile for the 51 nm thick Ce:YIG sample deposited on fused silica. Positive depths *d* represent the substrate and negative *d* the film. The vertical axis shows the peak area divided by the relative sensitivity factor (RSF) and was normalized with respect to specific peaks, i.e. the value of the Y 3d peak at a depth of $d = -15$ nm was used to normalize the Ce 3d, Y 3d, Fe 2p, and O 1s peaks, and the value of the OH^- peak at $d = 18$ nm was used to normalize the OH- data. The position of $d = 0$, i.e. the film/substrate interface, was determined from the intensity of the OH^- peak originating from the fused silica substrate, so that $d = 0$ corresponds to an intensity of half the maximum. The binding energy of O 1s attributed to the film is 529.2–530.4 eV, but that attributed to the fused silica substrate is 531.6–532.2 eV [41,42].

In Fig. 7c, the film region shows Ce 3d, Fe 2p, O 1s, Y 3p, Y 3d, Ce 4d, Fe 3p, and O 2s, and KLL and LMM Auger electrons attributed to Ce:YIG. Fig. 7d–i shows the XPS peaks at $d = -49$ nm, the etched top surface of the film. Fig. 7e is consistent with the Ce being present as Ce^{3+} not Ce^{4+}, corresponding to stoichiometric Ce:YIG with a large FR [20]. However, in the range of $d = -5$ to 2 nm near the interface, the amount of Fe 2p decreased compared with Y 3d, and the ratio of Fe 2p/Ce 3d reached a higher value than it does in the Ce:YIG layer (Fig. 7b). These data suggest that this interfacial region was not stoichiometric Ce:YIG, and its thickness is several nm, close to the value estimated from magnetic properties and TEM images.

The combined structural and chemical data therefore indicate the presence of a non-stoichiometric, amorphous interfacial layer above the silica. The optical absorption and the magnetooptical FOM as well as the magnetization decrease for the thinnest films. We hypothesize that the interfacial layer is responsible for the high absorption as a result of mixed valence cations and structural disorder [43,44], and also has a magnetization much smaller than that of the Ce:YIG layer, thereby degrading the FOM for thin films. On the other hand, the thickest films exhibit a reduced FOM resulting from cracking, leading to an optimum FOM at intermediate thicknesses of 300–500 nm.

4. Conclusions

Ce:YIG films with thicknesses of 51–2056 nm were fabricated on fused silica and on Si substrates by RF IBS and vacuum annealing. A 338 nm thick film showed the largest magnetooptical FOM, 127°/dB at a wavelength of 1550 nm, more than three times larger than prior work. The thickness dependence of magnetic and magnetooptical properties was not monotonic. Thin films exhibited a lower magnetization and increased optical absorption which we attribute to the effects of an amorphous interfacial layer of thickness approximately 5 nm formed at the boundary between the Ce:YIG and the silica substrate. The saturation magnetization of the interfacial layer is five times smaller than that of the stoichiometric Ce:YIG, and the optical absorption was three orders larger than that of Ce:YIG, dramatically reducing the magnetooptical figure of merit of the Ce:YIG film. In contrast, for thick films, cracking and delamination caused by thermal mismatch strain leads to a decrease in FOM. These results may be used to optimize the magnetooptical performance of Ce:YIG films. The interfacial layer may be eliminated or reduced by adjusting the composition of the initial few nm of the film, or the deposition conditions such as oxygen pressure to improve the stoichiometry of the film. The cracking may be reduced by using a substrate with closer thermal expansion compared to that of Ce:YIG, e.g. quartz instead of fused silica. These strategies may widen the window of thicknesses that yield films with a high FOM and contribute to the further development of magnetooptical devices based on polycrystalline Ce:YIG films.

CRediT authorship contribution statement

Yuki Yoshihara: Data curation, (lead), Formal analysis, (equal), Software, (lead). **Tomoya Sugita:** Data curation, (supporting), Formal analysis, (equal). **Pang Boey Lim:** Data curation, (supporting), Supervision, (supporting). **Yasuyuki Tamba:** Data curation, (supporting), Formal analysis, (supporting). **Hiroaki Inoue:** Data curation, (supporting), Formal analysis, (supporting). **Kazushi Ishiyama:** Validation, (supporting), Supervision, (supporting), Writing – review & editing, (supporting). **Mitsuteru Inoue:** Funding acquisition, (equal), Validation, (supporting). **Caroline A. Ross:** Validation, (lead), Writing – review & editing, (lead). **Taichi Goto:** Conceptualization, (lead), Formal analysis, (equal), Funding acquisition, (equal), Methodology, (equal), Project administration, (equal), Software, (equal), Supervision, (lead), Writing – original draft, (lead), Writing – review & editing, (equal).

Declaration of competing interest

The authors declare that they have no known competing financial interests or personal relationships that could have appeared to influence the work reported in this paper.

Data availability

Data will be made available on request.

Acknowledgments

This work was partly supported by Grants-in-Aid for Scientific Research (KAKENHI) Nos. 20H02593, 20K20535 from the Japan Society for the Promotion of Science (JSPS), Bilateral Program No. JPJSBP120214807 from JSPS and No. 21-52-50006 from RFBR, New Energy and Industrial Technology Development Organization (NEDO) No. 20002157, Tohoku Initiative for Fostering Global Researchers for Interdisciplinary Sciences (TI-FRIS) fellowship, the Foundation for Technology Promotion of Electronic Circuit Board, and the Tanaka Kikinzoku Memorial Foundation. We also acknowledge Prof. Yuichi Nakamura, Prof. Hironaga Uchida, and the Cooperative Research Facility Center at Toyohashi University of Technology for their support. CAR acknowledges support of NSF award ECCS2028199.

Appendix A. Supplementary data

Supplementary data related to this article can be found online at https://doi.org/10.1016/j.optmat.2022.112967.

References

[1] M. Inoue, M. Levy, A.V. Baryshev. Magnetophotonics from Theory to Applications, Springer, New York, 2014. https://doi.org/10.1007/978-3-642-35509-7.
[2] T. Goto, R. Morimoto, J.W. Pritchard, M. Mina, H. Takagi, Y. Nakamura, P.B. Lim, T. Taira, M. Inoue, Magneto-optical Q-switching using magnetic garnet film with micromagnetic domains, Opt. Express 24 (16) (2016), 17635, https://doi.org/10.1364/OE.24.017635.
[3] N. Adachi, K. Yogo, T. Ota, M. Takahashi, K. Ishiyama, Magneto-optical effect and ferromagnetic resonance of Bi–Fe garnet for high frequency electromagnetic sensor, J. Appl. Phys. 109 (7) (2011), 07A506, https://doi.org/10.1063/1.3556709.
[4] Y. Nakamura, P.B. Lim, T. Goto, H. Uchida, M. Inoue, Recording and reconstruction of volumetric magnetic hologram using multilayer medium with heat dissipation layers, Opt Express 27 (20) (2019), 27573, https://doi.org/10.1364/OE.27.027573.
[5] L. Bi, J. Hu, P. Jiang, D.H. Kim, G.F. Dionne, L.C. Kimerling, C.A. Ross, On-chip optical isolation in monolithically integrated non-reciprocal optical resonators, Nat. Photonics 5 (2011) 758, https://doi.org/10.1038/nphoton.2011.270.
[6] T. Ishibashi, T. Kawata, T.H. Johansen, J. He, N. Harada, K. Sato, Magneto-optical indicator garnet films grown by metal-organic decomposition method, J. Magn. Soc. Jpn. 32 (2) (2008) 150, https://doi.org/10.3379/msjmag.32.150.
[7] H. Takagi, K. Nakamura, T. Goto, P.B. Lim, M. Inoue, Magneto-optic spatial light modulator with submicron-size magnetic pixels for wide-viewing-angle holographic displays, Opt. Lett. 39 (11) (2014) 3344, https://doi.org/10.1364/OL.39.003344.
[8] M. Levy, R.M. Osgood Jr., H. Hegde, F.J. Cadieu, R. Wolfe, V.J. Fratello, Integrated optical isolators with sputter-deposited thin-film magnets, IEEE Photon. Technol. Lett. 8 (7) (1996) 903, https://doi.org/10.1109/68.502265.
[9] B.J.H. Stadler, T. Mizumoto, Integrated magneto-optical materials and isolators: a review, IEEE Photon. J. 6 (1) (2014), 0600215, https://doi.org/10.1109/JPHOT.2013.2293618.
[10] H. Shimizu, Y. Nakano, Fabrication and characterization of an InGaAsP/InP active waveguide optical isolator with 14.7 dB/mm TE mode nonreciprocal attenuation, J. Lightwave Technol. 24 (1) (2006) 38, https://doi.org/10.1109/JLT.2005.861135.

[11] C. Zhang, P. Dulal, B.J.H. Stadler, D.C. Hutchings, Monolithically-integrated TE-mode 1D silicon-on-insulator isolators using seedlayer-free garnet, Sci. Rep. 7 (1) (2017) 5820, https://doi.org/10.1038/s41598-017-06043-z.

[12] T. Goto, M.C. Onbasli, D.H. Kim, V. Singh, M. Inoue, L.C. Kimerling, C.A. Ross, A nonreciprocal racetrack resonator based on vacuum-annealed magnetooptical cerium-substituted yttrium iron garnet, Opt Express 22 (16) (2014), 19047, https://doi.org/10.1364/OE.22.019047.

[13] Y. Zhang, Q. Du, C. Wang, T. Fakhrul, S. Liu, L. Deng, D. Huang, P. Pintus, J. Bowers, C.A. Ross, J. Hu, L. Bi, Monolithic integration of broadband optical isolators for polarization-diverse silicon photonics, Optica 6 (4) (2019) 473, https://doi.org/10.1364/OPTICA.6.000473.

[14] Q. Du, C. Wang, Y. Zhang, Y. Zhang, T. Fakhrul, W. Zhang, C. Gonçalves, C. Blanco, K. Richardson, L. Deng, C.A. Ross, L. Bi, J. Hu, Monolithic on-chip magneto-optical isolator with 3 dB insertion loss and 40 dB isolation ratio, ACS Photonics 5 (12) (2018) 5010, https://doi.org/10.1021/acsphotonics.8b01257.

[15] R. Ma, S. Reniers, Y. Shoji, T. Mizumoto, K. Williams, Y. Jiao, J. van der Tol, Integrated polarization-independent optical isolators and circulators on an InP membrane on silicon platform, Optica 8 (12) (2021) 1654, https://doi.org/10.1364/OPTICA.443097.

[16] M.C. Onbasli, L. Beran, M. Zahradník, M. Kučera, R. Antoš, J. Mistrík, G.F. Dionne, M. Veis, C.A. Ross, Optical and magneto-optical behavior of cerium yttrium iron garnet thin films at wavelengths of 200–1770 nm, Sci. Rep. 6 (2016), 23640, https://doi.org/10.1038/srep23640.

[17] T. Goto, Y. Eto, K. Kobayashi, Y. Haga, M. Inoue, C.A. Ross, Vacuum annealed cerium-substituted yttrium iron garnet films on non-garnet substrates for integrated optical circuits, J. Appl. Phys. 113 (17) (2013) 17A939, https://doi.org/10.1063/1.4800946.

[18] M. Gomi, K. Satoh, H. Furuyama, M. Abe, Sputter deposition of Ce-substituted iron garnet films with giant magneto-optical effect, J. Magn. Soc. Jpn. 13 (2) (1989) 163, https://doi.org/10.3379/jmsjmag.13.163.

[19] X. Zhou, F. Lin, X. Ma, W. Shi, Fabrication and magnetic properties of $Ce_1Y_2Fe_5O_{12}$ thin films on GGG and SiO_2/Si substrates, J. Magn. Magn Mater. 320 (12) (2008) 1817, https://doi.org/10.1016/j.jmmm.2008.02.169.

[20] T. Yoshimoto, T. Goto, R. Isogai, Y. Nakamura, H. Takagi, C.A. Ross, M. Inoue, Magnetophotonic crystal with cerium substituted yttrium iron garnet and enhanced Faraday rotation angle, Opt Express 24 (8) (2016) 8746, https://doi.org/10.1364/OE.24.008746.

[21] W.E. Ross, D. Psaltis, R.H. Anderson, Two-dimensional magneto-optic spatial light modulator for signal processing, Opt. Eng. 22 (4) (1983) 485, https://doi.org/10.1117/12.7973148.

[22] P. Jae-Hyuk, S. Il-Kwon, C. Jae-Kyeong, K. Nishimura, H. Uchida, M. Inoue, Flat-surface pixel for magneto-optic spatial light modulator, IEEE Trans. Magn. 39 (5) (2003) 3169, https://doi.org/10.1109/TMAG.2003.816046.

[23] K. Aoshima, H. Kinjo, K. Machida, D. Kato, K. Kuga, T. Ishibashi, H. Kikuchi, Active matrix magneto-optical spatial light modulator driven by spin-transfer-switching, J. Disp. Technol. 12 (10) (2016) 1212, https://doi.org/10.1109/JDT.2016.2591061.

[24] V. Marinova, S.H. Lin, S. Petrov, M.S. Chen, Y.H. Lin, K.Y. Hsu, Graphene-based spatial light modulator operating at near infrared spectral range, Appl. Surf. Sci. 472 (2019) 2, https://doi.org/10.1016/j.apsusc.2018.09.150.

[25] R. Morimoto, T. Goto, T. Taira, J. Pritchard, M. Mina, H. Takagi, Y. Nakamura, P. B. Lim, H. Uchida, M. Inoue, Randomly polarised beam produced by magnetooptically Q-switched laser, Sci. Rep. 7 (1) (2017), 15398, https://doi.org/10.1038/s41598-017-15826-3.

[26] R. Morimoto, T. Goto, Y. Nakamura, P.B. Lim, H. Uchida, M. Inoue, Crystalline and magnetooptical characteristics of $(Tb,Bi)_3(Fe,Ga)_5O_{12}$ deposited on $(Y,Nd)_3Al_5O_{12}$, Jpn. J. Appl. Phys. 57 (6) (2018), 061101, https://doi.org/10.7567/JJAP.57.061101.

[27] T. Taira, A. Mukai, Y. Nozawa, T. Kobayashi, Single-mode oscillation of laser-diode-pumped Nd:YVO_4 microchip lasers, Opt. Lett. 16 (24) (1991) 1955, https://doi.org/10.1364/OL.16.001955.

[28] J.J. Zayhowski, C. Dill, Diode-pumped passively Q-switched picosecond microchip lasers, Opt. Lett. 19 (18) (1994) 1427, https://doi.org/10.1364/OL.19.001427.

[29] N. Fairley, V. Fernandez, M. Richard-Plouet, C. Guillot-Deudon, J. Walton, E. Smith, D. Flahaut, M. Greiner, M. Biesinger, S. Tougaard, D. Morgan, J. Baltrusaitis, Systematic and collaborative approach to problem solving using X-ray photoelectron spectroscopy, Applied Surface Science Advances 5 (2021), 100112, https://doi.org/10.1016/j.apsadv.2021.100112.

[30] M. Bonnet, A. Delapalme, H. Fuess, M. Thomas, Refinement of the structure of yttrium iron garnet (YIG). A case of severe extinction and absorption, Acta Crystallogr. B 31 (9) (1975) 2233, https://doi.org/10.1107/S0567740875007315.

[31] S. Geller, G.P. Espinosa, P.B. Crandall, Thermal expansion of yttrium and gadolinium iron, gallium and aluminum garnets, J. Appl. Crystallogr. 2 (2) (1969) 86, https://doi.org/10.1107/S0021889869006625.

[32] B. Kühn, R. Schadrack, Thermal expansion of synthetic fused silica as a function of OH content and fictive temperature, J. Non-Cryst. Solids 355 (4–5) (2009) 323, https://doi.org/10.1016/j.jnoncrysol.2008.11.005.

[33] T. Yoshimoto, T. Goto, H. Takagi, Y. Nakamura, H. Uchida, C.A. Ross, M. Inoue, Thermally stable amorphous tantalum yttrium oxide with low IR absorption for magnetophotonic devices, Sci. Rep. 7 (1) (2017), 13805, https://doi.org/10.1038/s41598-017-14184-4.

[34] M. Born, E. Wolf. Principles of Optics: Electromagnetic Theory of Propagation, Interference and Diffraction of Light, 7 ed., Cambridge University Press, Cambridge, 1999. https://doi.org/10.1017/CBO9781139644181.

[35] T. Shintaku, A. Tate, S. Mino, Ce-substituted yttrium iron garnet films prepared on $Gd_3Sc_2Ga_3O_{12}$ garnet substrates by sputter epitaxy, Appl. Phys. Lett. 71 (12) (1997) 1640, https://doi.org/10.1063/1.120003.

[36] E. Lage, L. Beran, A.U. Quindeau, L. Ohnoutek, M. Kucera, R. Antos, S.R. Sani, G. F. Dionne, M. Veis, C.A. Ross, Temperature-dependent Faraday rotation and magnetization reorientation in cerium-substituted yttrium iron garnet thin films, APL Mater. 5 (3) (2017), 036104, https://doi.org/10.1063/1.4976817.

[37] T. Goto, M.C. Onbasli, C.A. Ross, Magneto-optical properties of cerium substituted yttrium iron garnet films with reduced thermal budget for monolithic photonic integrated circuits, Opt Express 20 (27) (2012), 28507, https://doi.org/10.1364/OE.20.028507.

[38] L. Bi, J. Hu, G.F. Dionne, L. Kimerling, C.A. Ross, Presented at the SPIE Proceedings San Francisco, California, USA Monolithic integration of chalcogenide glass/iron garnet waveguides and resonators for on-chip nonreciprocal photonic devices, Proc. SPIE 7941 (2011) 794105, https://doi.org/10.1117/12.875184.

[39] P. Ghising, Z. Hossain, R.C. Budhani, Stripe magnetic domains in $CeY_2Fe_5O_{12}$ (Ce:YIG) epitaxial films, Appl. Phys. Lett. 110 (1) (2017), 012406, https://doi.org/10.1063/1.4973481.

[40] T. Yoshimoto, T. Goto, K. Shimada, B. Iwamoto, Y. Nakamura, H. Uchida, C. A. Ross, M. Inoue, Static and dynamic magnetic properties of single-crystalline yttrium iron garnet films epitaxially grown on three garnet substrates, Adv. Electron. Mater. 4 (2018), 1800106, https://doi.org/10.1002/aelm.201800106.

[41] Z. Simsa, J. Zemek, XPS investigation of LPE garnet films, Czech. J. Phys. 40 (11) (1990) 1274, https://doi.org/10.1007/BF01605056.

[42] S.M. Suturin, A.M. Korovin, V.E. Bursian, L.V. Lutsev, V. Bourobina, N.L. Yakovlev, M. Montecchi, L. Pasquali, V. Ukleev, A. Vorobiev, A. Devishvili, N.S. Sokolov, Role of gallium diffusion in the formation of a magnetically dead layer at the $Y_3Fe_5O_{12}$/$Gd_3Ga_5O_{12}$ epitaxial interface, Phys. Rev. Mater. 2 (10) (2018), 104404, https://doi.org/10.1103/PhysRevMaterials.2.104404.

[43] A. Schlegel, S.F. Alvarado, P. Wachter, Optical properties of magnetite Fe_3O_4, J. Phys. C Solid State Phys. 12 (6) (1979) 1157, https://doi.org/10.1088/0022-3719/12/6/027.

[44] X. Guo, A.H. Tavakoli, S. Sutton, R.K. Kukkadapu, L. Qi, A. Lanzirotti, M. Newville, M. Asta, A. Navrotsky, Cerium substitution in yttrium iron garnet: valence state, structure, and energetics, Chem. Mater. 26 (2) (2014) 1133, https://doi.org/10.1021/cm403444f.